Improved quantitation for PET/CT image reconstruction with system modeling and anatomical priors

Adam M. Alessio[a] and Paul E. Kinahan
Department of Radiology, University of Washington Medical Center, 200 Old Fisheries Center, Box 357987, Seattle, Washington 98195-7987

(Received 27 March 2006; revised 21 June 2006; accepted for publication 4 September 2006; published 17 October 2006)

Accurate quantitation of positron emission tomography (PET) tracer uptake levels in tumors is important for staging and monitoring response to treatment. Quantitative accuracy in PET is particularly poor for small tumors because of system partial volume errors and smoothing operations. This work proposes a reconstruction algorithm to reduce the quantitative errors due to limited system resolution and due to necessary image noise reduction. We propose a method for finding and using the detection system response in the projection matrix of a statistical reconstruction algorithm. In addition, we use aligned anatomical information, available in PET/CT scanners, to govern the penalty term applied during each image update. These improvements are combined with Fourier rebinning in a clinically feasible algorithm for reconstructing fully three-dimensional PET data. Results from simulation and measured studies show improved quantitation of tumor values in terms of bias and variance across multiple tumor sizes and activity levels with the proposed method. At common clinical image noise levels for the detection task, the proposed method reduces the error in maximum tumor values by 11% compared to filtered back-projection and 5% compared to conventional iterative methods. © *2006 American Association of Physicists in Medicine*.
[DOI: 10.1118/1.2358198]

Key words: PET/CT, anatomical priors, system modeling, PET reconstruction, detector response

I. INTRODUCTION

The quantitative accuracy of reconstructed positron emission tomography (PET) images is limited by the spatial resolution of the imaging system and the number of photons collected. System acquisition physics, including detector geometry, intercrystal scatter, depth-dependent sensitivity, and crystal penetration influence the overall resolution of a scanner, resulting in a spatially variant and nonideal resolution response. Moreover, PET imaging suffers from a limited number of photons resulting in noisy images that require some form of implicit or explicit smoothing operation. Both of these effects degrade the quantitative accuracy of modern PET scanners.

In order to emphasize the problems with tumor quantitation, we generated analytical simulations of a fluorine-18 PET scan of a cylindrical phantom, which contained spherical targets of diameters ranging from 0.5 to 3 cm. The contrast ratio of targets to background was 8:1. Poisson noise was added to the raw sinograms to create 50 noisy realizations, each simulating a 5 min scan. The sinograms were corrected for attenuation and reconstructed using ordered subset expectation maximization (OSEM) at a resolution of $256 \times 256 \times 63$ voxels. We calculated the normalized bias in each target of these reconstructions as the true target value minus the mean of the activity concentration values in the target volume divided by the true target value. Figure 1 presents the average of the normalized bias across all realizations. The mean activity concentration values of small tumors (0.5 cm diameter) are as much as 80% below their true value. The nonideal system resolution causes partial volume errors even in relatively large tumors (3 cm diameter), as evident in the OSEM reconstruction with no post-smoothing. In practice, images reconstructed with OSEM are post-smoothed, which further degrades tumor quantitation. This work offers solutions to address both of these causes of quantitative error.

We propose using accurate system modeling and anatomical information in a clinically feasible reconstruction algorithm to reduce quantitative errors. The use of a system model accounting for the detection system response improves the spatial resolution of the reconstructions. Accurate system models, with varying levels of complexity, have been successfully applied to high-resolution small-animal PET systems.[1–6] Previous research has characterized the spatially variant system response in terms of coincident aperture functions,[7] system kernels,[1] detector response functions,[2] and detector blurring terms.[3,8] Our work employs a more general response that models both the detection process and the effects of Fourier rebinning (FORE). Therefore, our modified method uses a more general "system response function" (SRF).

Past efforts have characterized the system response of small-animal PET tomographs with varying methods. Several studies have employed analytical derivations to determine theoretical response functions.[2,5–7,9] A potentially more accurate although more labor intensive approach is to measure the response function of an actual system.[1,8] A compromise in terms of accuracy uses Monte Carlo simulations to model the tomograph.[3,10,11] This work uses Monte Carlo

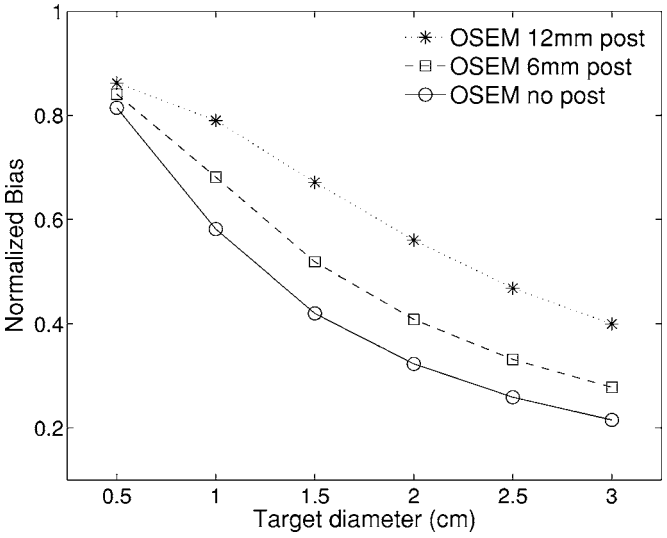

FIG. 1. Bias in mean tumor value versus tumor diameter highlights quantitative inaccuracies with conventional reconstruction approach of performing OSEM and post-smoothing with 6 and 12 mm three-dimensional Gaussian filters.

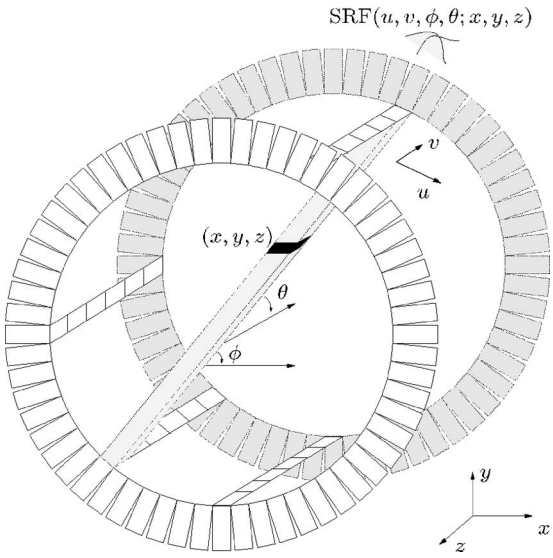

FIG. 2. Illustration of fully characterized system response function SRF, where (u,v) defines the point on one detector surface where the coincident bin with azimuthal and axial angle (ϕ,θ) intersects. In addition, (x,y,z) defines the location in the volume that contributes to this coincident bin.

methods to model physical effects such as crystal penetration and intercrystal scatter present in a whole-body, human PET system.

Along with an accurate system model, we propose a method for image variance reduction with the aid of anatomical information. Current reconstruction algorithms perform some form of smoothing operation to reduce the variance levels in PET images at the expense of increased bias.[12] A common approach is the iterative algorithm OSEM. This algorithm stops the iterative process prematurely to implicitly reduce variance and then post-smooths the image to explicitly reduce variance. This reduction of variance/noise increases the bias in the estimated image.

PET/CT scanners offer the added advantage of aligned anatomical information that can be incorporated into the emission reconstruction algorithm to reduce image smoothness near the boundaries of tumors. Based on the assumption that the reconstructed CT image provides useful information about the boundary of emission regions, this improvement allows for desirable noise properties in limited photon count scans while maintaining accurate tumor uptake levels. Several studies have explored the benefits of using anatomical information to guide reconstruction and noise regularization.[13–16] In particular, the use of CT-derived boundary information to improve quantitation was investigated by Comtat *et al.*[17]

We have previously presented a thorough discussion of our system response modeling and its influence in the OSEM reconstruction.[18] This work expands these efforts with the addition of anatomical side information in a modified penalized reconstruction algorithm to address the two major causes of quantitative inaccuracy.

II. SYSTEM RESPONSE FUNCTION

In a complete model, a whole-body PET system can be described by a seven-dimensional function with four dimensions to describe the line integral domain and three dimensions to describe the spatial coordinates of the imaging volume. One choice of variables appears in Fig. 2 to describe SRF $(u,v,\phi,\theta;x,y,z)$, where (u,v) defines the point on one detector surface where the coincident bin with azimuthal and axial angle (ϕ,θ) intersects. In addition (x,y,z) defines the location in the volume that contributes to this coincident bin.

The system model for a PET tomograph can be factorized into multiple components such as the geometric projection matrix (basis for all conventional models), attenuation correction factors, detector sensitivity factors, and detector blurring.[10] This work models the detector blurring component as a spatially variant response function that influences the other factors of the system model. Even though iterative reconstructions can accommodate sophisticated and accurate detector blurring models, all current clinical PET systems use spatially invariant approaches during reconstruction. In other words, they use a one-dimensional system response function. Past efforts to model a spatially variant detector blurring factor in high-resolution research systems often use the two-dimensional function, $S_{2\text{Dsimple}}(s;s_v)$, which blurs along radial bins in the sinograms (s, the distance between the z axis and the projection of the line onto a transaxial plane) and is spatially variant in radial distance s_v. The subscript v denotes the variables that parameterize the originating volume location as opposed to the line integrals. We will term this two-dimensional (2-D) function as a "1+1" because it blurs in one dimension and is variant in one dimension. Figure 3 presents the rationale for such a detector response function showing that is can account for radial nonuniform sinogram spacing, crystal penetration, and intercrystal scatter. This research employs a more complicated 2+1 SRF, which blurs in two dimensions and is variant in one dimension.

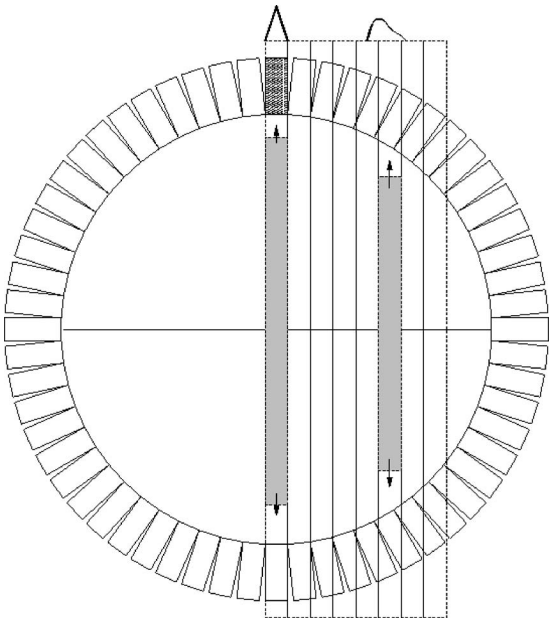

FIG. 3. Depiction of the need for a 1+1 SRF. Photons from sinogram bins at edge of field of view can contribute to multiple detectors and be binned into erroneous sinogram bins. This $S_{2Dsimple}(s;s_v)$ blurs measurements in radial position and is variant in radial position.

We employed Monte Carlo techniques to model the detection system of a fully three-dimensional (3-D) PET scanner.[19] We then performed Fourier rebinning (FORE) of the fully 3-D data to reduce the data size leading to a clinically feasible reconstruction algorithm.[20] The seven-dimensional function describing this process was simplified to a three-dimensional SRF. Specifically, we found the 2+1 $S(s,z;s_v)$ which blurs the ideal system matrix along radial bins (s) and axial planes (z) and is variant along radial bins (s_v). These dimensions were chosen from visual inspection of the resolution degradation in the data domain formed from point sources placed throughout the imaging volume. The radial bins followed by the axial bins received the greatest degradation and the response was influenced most by the radial positioning of the source. Figure 4 displays the simulated SRF at varying radial positions. A detailed description of the simulation and application of the system response function appears in our previous work.[18]

III. ANATOMICAL BOUNDARY INFORMATION

PET/CT systems offer the added advantage for PET reconstruction of an aligned anatomical map. The anatomical map from the CT could be used in a variety of ways to govern image smoothness with the desire of reducing partial volume effects and improving quantitative accuracy. Our past work explored using anatomical information post-reconstruction to improve upon conventional OSEM post-processing.[21] This work uses the CT data during the reconstruction.

In practice, segmenting the CT image, to provide anatomical boundary information, is potentially a difficult problem. Several methods have been implemented (e.g.[22,23]), which typically use amplitude, shape, and texture information to automatically detect regions of interest. Advanced methods such as level sets[24] run into difficulties with low image signal-to-noise ratio that can lead to missing boundary information. To address these difficulties, deformable models have been used successfully to increase robustness, which can be further improved by using *a priori* anatomical knowledge to describe shape variations.[25] While automatic methods are desirable, such approaches often have reduced sensitivity and/or specificity compared to operator-guided approaches. Alternatively, in the "just-enough-information" (JEI) approach, a physician interacts with the segmentation algorithm as little as possible while still ensuring clinically

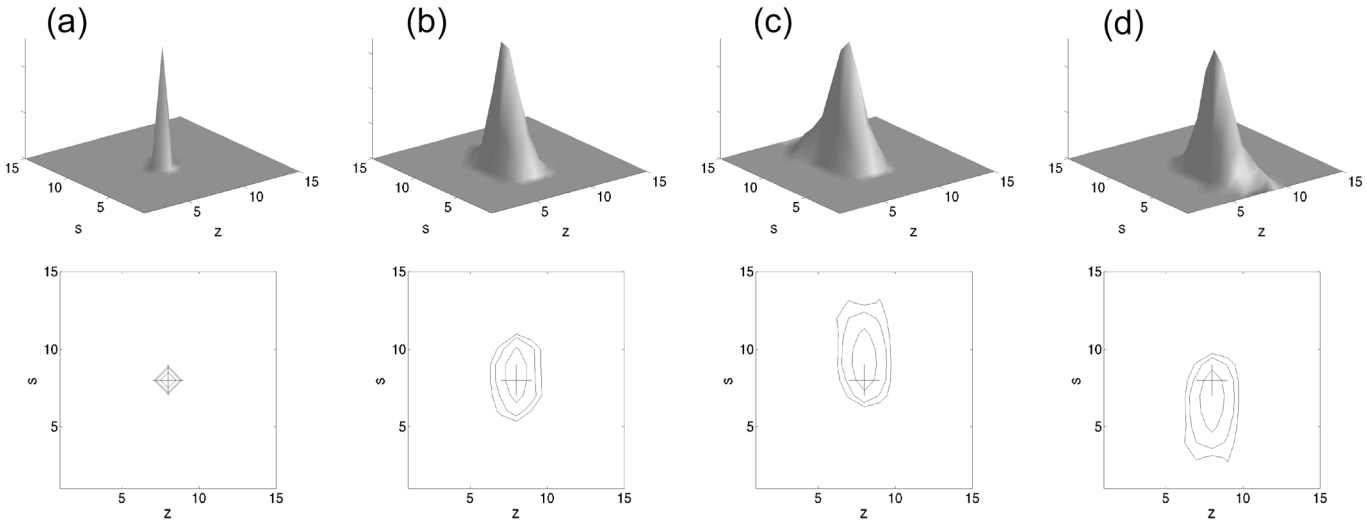

FIG. 4. $S(s,z;s_v)$ at different radial locations s_v for a transaxial FOV $[-27.5\text{ cm}, 27.5\text{ cm}]$. The second row presents the SRF as contour plots showing half, fifth, and tenth maximum contours, and marking the center of SRF from an ideal system with a cross. (a) Ideal $S(s,z)$ for all s_v; (b) $S(s,z;s_v=0\text{ cm})$; (c) $S(s,z;s_v=-20\text{ cm})$; (d) $S(s,z;s_v=+20\text{ cm})$.

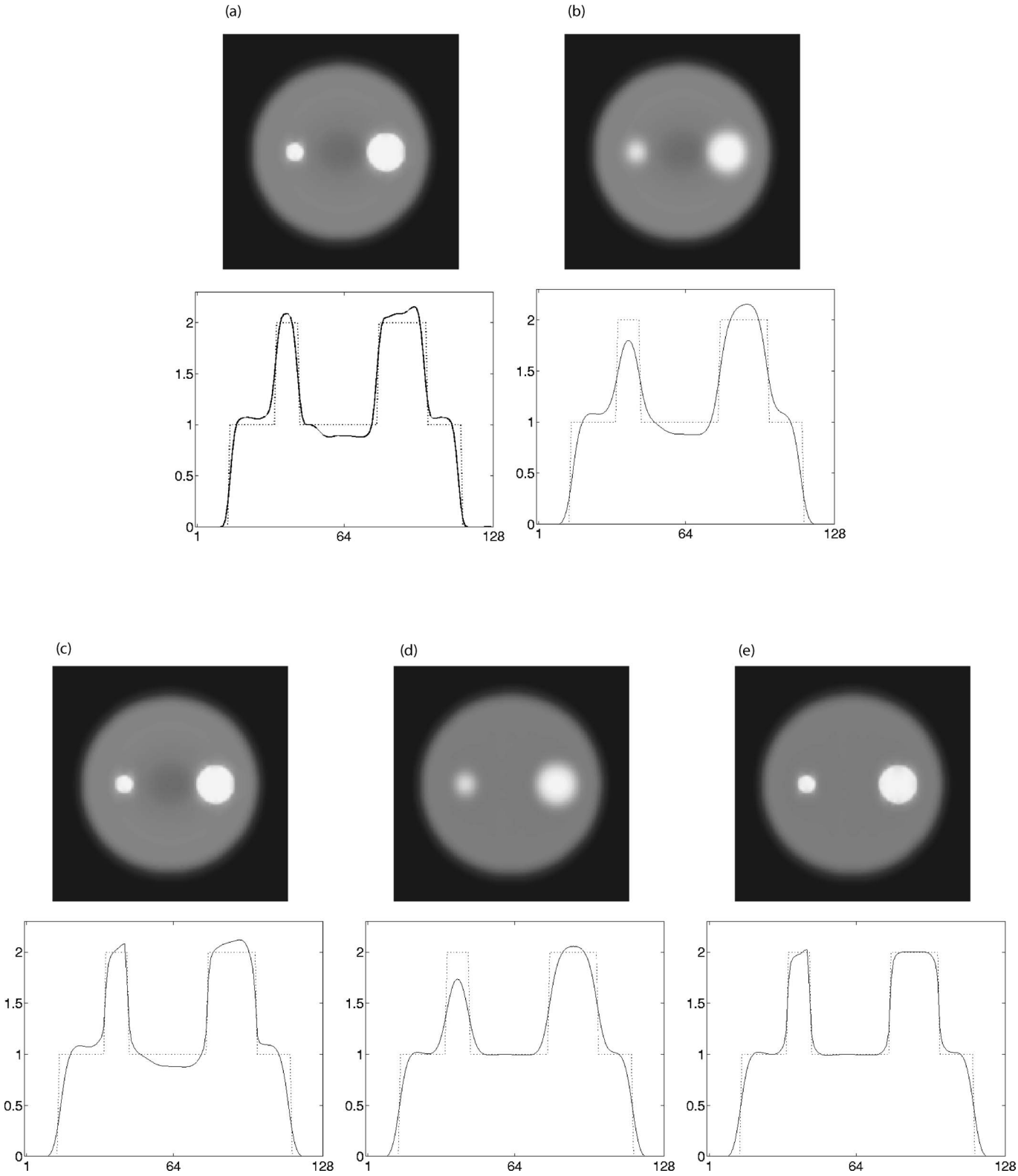

FIG. 5. Noiseless 2-D sample case showing benefit of system response function and boundary prior information in the reconstruction. Each reconstruction is displayed with a horizontal profile through the reconstruction (solid line) and through the true object (dotted line). (a) FBP 10 mm Hanning window. (b) Conventional PWLS. (c) PWLS+boundary info. (d) PWLS+SRF. (e) PWLS+SRF and boundary info.

acceptable results. Minimizing physician input with the JEI approach reduces processing time and intra- and interoperator variability.[26]

Another challenge is that anatomical boundaries do not necessarily coincide with emission boundaries in the PET image. For example, in radiation treatment planning, it is a

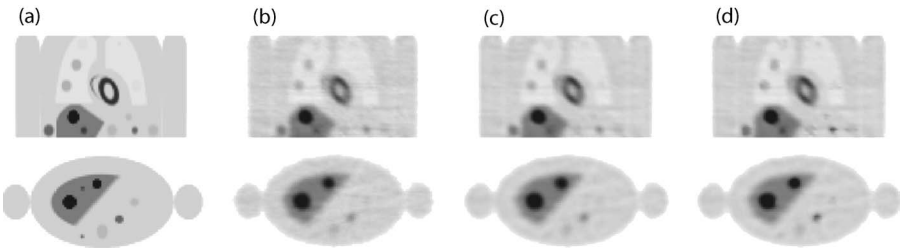

FIG. 6. Coronal and transaxial slices through reconstructions of a single noise realization of the simulated anthropomorphic phantom. (a) True image. (b) Conventional PWLS. (c) PWLS+S_{2+1}. (d) PWLS+S_{2+1} and boundary info.

well appreciated fact that tumor boundary definitions derived from CT images and flourodeoxyglucose PET images are not identical in 15%–60% of patients with non-small cell lung cancer.[27–29]

This current work seeks to quantify the benefit of functional boundary information and determine if it is worth researching functional boundary segmentation for improved PET image reconstruction. This work assumes that we can perform an accurate segmentation of aligned CT images to supply approximate boundary information of radionuclide uptake regions, providing *a priori* image smoothness information. Specifically, in the simulation examples presented here, edge detection was performed to find the boundary regions of known tumor locations (provided by anatomic CT image). These regions were grown to approximately match the system resolution. The regions were then blurred with a 3-D Gaussian to reduce errors from potential, minor spatial mismatch.[17] Finally, these blurred regions defined the strength of a quadratic penalty term used in a penalized weighted least-squares (PWLS) method.[30]

IV. METHODS

A. Application

The improved SRF and boundary information were incorporated into the PWLS similarity measure

$$\Phi_{\mathrm{PWLS}}(x) = \tfrac{1}{2}(y - \mathbf{P}x)'\mathbf{W}(y - \mathbf{P}x) + \beta(x)G(x), \tag{1}$$

where the system matrix $\mathbf{P}$ times the estimate of the image (x) provides the current estimate of the conditional mean of the data (y). The weighting matrix $\mathbf{W}$ is the inverse of an estimate of the conditional variances of the data.[30] The regularization term $G(x)$ used for this study is the quadratic penalty

$$G(x_i) = \sum_{k \in N_{3D_i}} \frac{(x_i - x_k)^2}{d_{ik}}, \tag{2}$$

where d_{ik} is the Euclidean distance between voxels i and k. The strength of the regularization term β varies based on the boundary information. That is, β is less in boundary regions to preserve edges and is greater in constant activity regions. For the applications presented here, β varies smoothly from 100% to 10% of its full value at the boundary of a tumor region. We denote the full value of β as the "global" prior term. Finally, the objective function (1) was optimized with iterative coordinate decent.[31]

The improved SRFs are incorporated into the system matrix $\mathbf{P}$. Since system memory and algorithm optimization was not a concern in this study, the system matrix was precomputed and blurred with the corresponding SRF. When $S(s,z;s_v)$ was used, the method is termed "PWLS+S_{2+1}." For comparison, the more simple $S(s;s_v)$ was also used and is termed "PWLS+S_{1+1}."

These methods were applied to 2-D PET data (Fourier rebinned fully 3-D measurements). It should be stressed that PWLS+S_{2+1} method is not a strict 2-D reconstruction algorithm in that it requires neighboring transaxial slices during the reconstruction of a single transaxial slice. Therefore, instead of iterating on a single transaxial slice, finding the final image estimate, and moving to the next transaxial slice, as is done in conventional 2-D PET reconstruction, this method performs one iteration for all of the transaxial slices, and then performs the next iteration for all of the transaxial slices. To improve performance, the order of which transaxial slice is updated changes with each iteration.

B. Simulations of noiseless 2-D phantom

The proposed methods were first applied to data from a simple simulated phantom containing a constant background

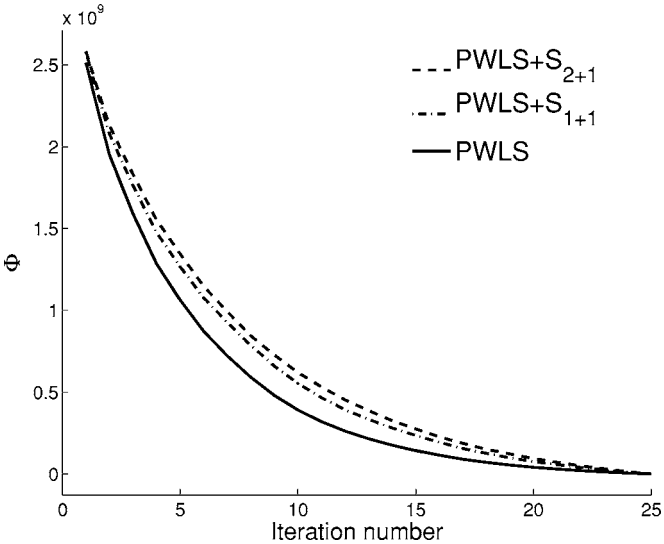

FIG. 7. Convergence for proposed methods methods plotting Φ_{PWLS} vs iteration number of the PWLS algorithms used with whole-body PET measurements. Convergence is slightly slower when the system response function is included.

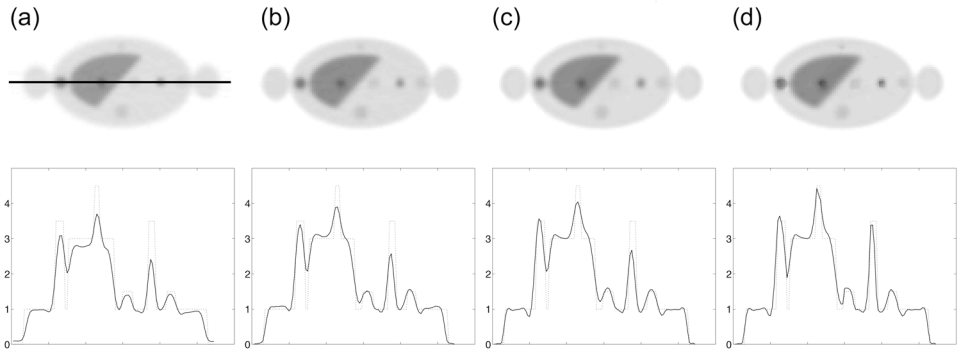

FIG. 8. Transaxial slice through mean images of 50 noise realizations. The second row plots the horizontal profile through the slice with a solid line and the profile through the true object with a dotted line. (a) FBP. (b) conventional PWLS. (c) PWLS+S_{2+1}. (d) PWLS +S_{2+1} and boundary info.

and two hot spots with a 2:1 contrast ratio. Noiseless 2-D data were generated from the phantom and were modified to account for intercrystal scatter and crystal penetration present in a whole-body scanner. This simple simulation study offers insights into the basic behavior of the proposed methods.

C. Simulations of anthropomorphic phantom

The methods were tested with analytically generated fully 3-D measurements[32] from a whole-body phantom imaged in a scanner with a geometry similar to the GE Advance.[33] The phantom represents a typical body size (90 cm waistline) and contained 24 spherical lesions of varying sizes (1 cm, 2 cm, and 3 cm diameters) and contrast levels (3.5:1 and 1.5:1) in varying background levels. Fully 3-D projections through the chest region of the phantom were calculated over two axial fields of view. We added typical clinical noise levels to these projections to contain 36% true, 36% random, and 28% scattered events with a total of 110×10^6 events per field of view. The simulation also modeled photon attenuation. After correcting the data in the fully 3-D domain, the measurements were FORE rebinned in preparation for 2-D image reconstruction. This simulation design allows for multiple independent noise realizations of the data sets in order to perform a thorough bias versus variance analysis. We simulated 50 noise realizations of the fully 3-D measurements.

These 50 noise realizations were reconstructed with conventional methods and with the proposed methods with a wide range of smoothing parameters. Several figures of merit were computed from these reconstructions including the root mean square error (RMSE) of the activity values in the tumor volume of interest (voxels fully inscribed in tumor) defined as

$$\mathrm{RMSE}_{r,l}=\sqrt{\sum_{i\in N_l}\frac{(x_i^T-x_{r,i})^2}{N_l}}, \tag{3}$$

where x_i^T is the i voxel of the true image and $x_{r,i}$ is the voxel from the reconstruction of realization r. The set of voxels in tumor, l, is N_l. The $\mathrm{RMSE}_{r,l}$ is averaged over all 50 realizations ($r=1\rightarrow50$) and then averaged over all 24 tumor regions ($l=1\rightarrow24$) to find the RMSE of the features. The average RMSE of background regions (voxels exterior to all tumor regions and interior to body) across all realizations was computed in the similar manner as (3).

The maximum and mean standardized uptake value of the tumor region of interest represents a common clinical task where accurate imaging quantitation is essential.[34] For this work we compute the bias in the maximum tumor values as

$$\mathrm{BiasMax}_{r,l}=\frac{x_l^T-\max\{x_r,N_l\}}{x_l^T}, \tag{4}$$

where x_l^T is the true value of the l tumor and x_r,N_l are all the values of the voxels in the l tumor of reconstruction r. As with the RMSE term, this value is averaged over all 50 realizations and then averaged over the 16 smaller tumors (1 cm and 2 cm diameter) since we are more concerned with improving quantitation for smaller lesions. To determine the precision of these terms, we also compute the variance in the maximum tumor values by finding the variance across all 50 realizations, as opposed to the mean across the 50 realizations. Similarly, we compute the bias in the mean tumor values by replacing the "max" operation in Eq. (4) with a "mean" operation.

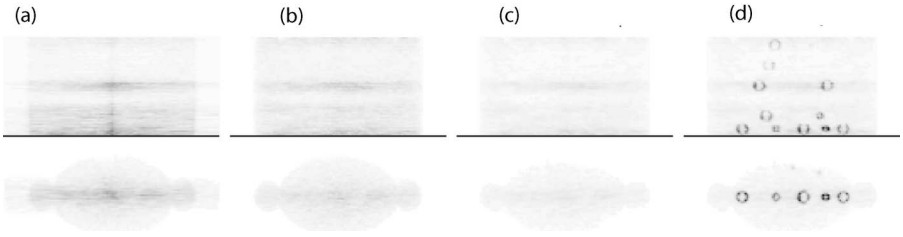

FIG. 9. Coronal slice (first row) and transaxial slice (second row) through variance images of 50 noise realizations. (a) FBP. (b) Conventional PWLS. (c) PWLS+S_{2+1}. (d) PWLS +S_{2+1} and boundary info.

D. Measured NEMA IEC body phantom

We also tested the methods with the NEMA IEC body phantom (Data Spectrum Corp, Chapel Hill, NC) imaged on a GE Advance scanner.[33] The phantom consists of six spheres (3.7 to 1.0 cm diameters) suspended in a semi-anthropomorphic chamber. The spheres and chamber contained F18 with a sphere to background activity concentration ratio of 8:1. Fully 3-D data sets were collected from the phantom for 5 min in one bed position with a total of 3×10^7 events. These data were fully corrected and Fourier rebinned prior to offline reconstruction.

V. RESULTS AND DISCUSSION

A. Noiseless 2-D phantom

Figure 5 presents reconstructions from the simple 2-D phantom. Profiles through the reconstruction highlight the resolution and quantitative accuracy of the methods. The PWLS methods used the same global regularization strength. The PWLS with boundary information in the prior dramatically improves the edges of the tumors. The PWLS+SRF improved the accuracy of the background and tumor levels. The combination of the SRF and boundary information yielded the best results in edge preservation and tumor levels.

B. Anthropomorphic phantom

Figure 6 displays reconstructions using the different methods tested with the whole-body phantom. Images were chosen with similar noise properties. Filtered back-projection (FBP) was performed with a 10 mm Hanning filter and all of the PWLS reconstructions used the same global prior term and were iterated to convergence (25 iterations).

One might assume that the modified system matrix would require many more iterations to reach convergence since this results in a more ill-posed problem.[35] However, for this work the convergence rate is only slightly affected as shown in Fig. 7. The SRFs in whole-body imaging only slightly modify the geometric system matrix, resulting in slight changes in overall convergence rates, as opposed to the larger SRFs needed in a high-resolution system (smaller crystals leading to greater influence of crystal penetration and scatter effects).

Figure 8 displays the mean images from 50 reconstructions of the 50 different noise realizations. The smoothing parameter for each method was set to have similar variance levels in the images. The second row of the figure plots profiles through five tumors in the images along with the profile of the true object. The use of the SRF slightly improves the quantitation over conventional PWLS and the use of the SRF and boundary information greatly improves the quantitation in this single slice. These improvements in the PWLS+S and boundary method come at the expense of increased variance in the boundary regions as shown in the variance images in Fig. 9.

Figure 10 presents average RMSE values for tumor regions versus the average RMSE of the background region.

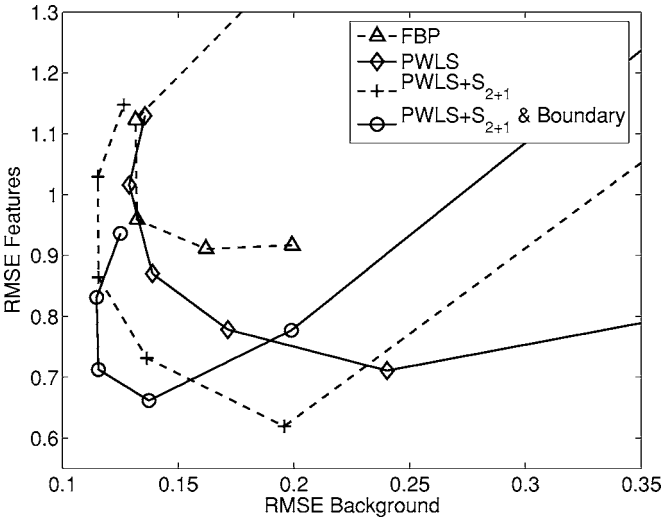

FIG. 10. Analysis of error in whole-body simulated phantom reconstructions as function of smoothing parameter. RMSE of features versus RMSE of background for FBP, conventional PWLS, PWLS+S_{2+1}, and PWLS+S_{2+1} and boundary information. Each datum is computed as the average RMSE of 24 features across 50 noise realizations.

Recall that each datum point was computed from 50 whole-body reconstructions and represents the average over 24 tumors. Entries close to the origin provide better performance in terms of this figure of merit. The conventional PWLS provides less RMSE than FBP at some background error levels. The PWLS+S_{2+1} method provides less RMSE then conventional PWLS at all variance levels and the addition of the boundary information offers the best performance tumor error with the least background error.

Figure 11 plots the bias in max tumor values versus the variance in the max values. A vertical line is plotted through

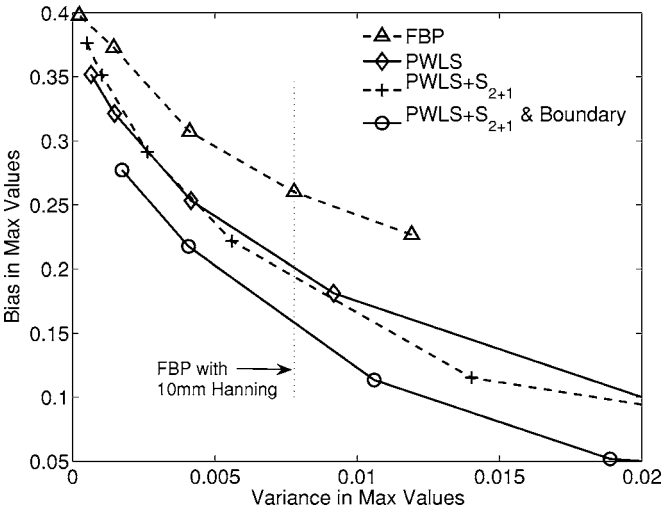

FIG. 11. Comparison of accuracy in max tumor values from whole-body simulations. Mean bias of max tumor values versus variance of max values across 50 realizations averaged over 16 1-cm- and 2-cm- diameter tumors. The curves are formed from varying the smoothing parameter for each method (cutoff of Hanning window for FBP and β for PWLS methods).

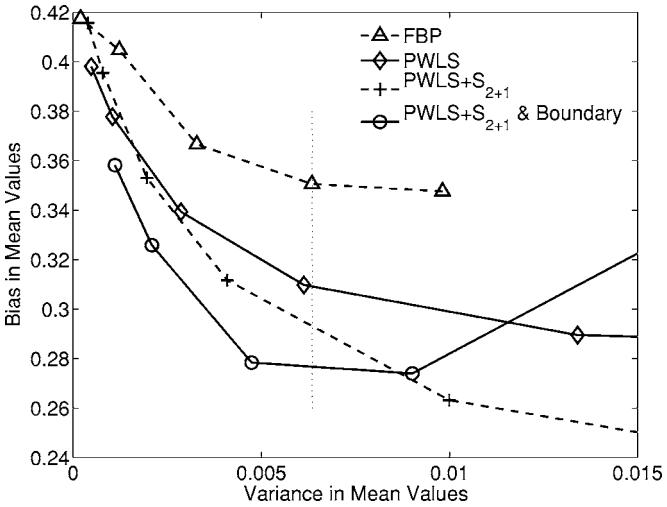

FIG. 12. Comparison of accuracy in mean tumor values from whole-body simulations. Mean bias of mean tumor values versus variance of mean values across 50 realizations averaged over 16 1-cm- and 2-cm-diameter tumors. The curves are formed from varying the smoothing parameter for each method.

the FBP with the 10 mm Hanning window (common clinical protocol for the detection task) to provide a frame of reference for expected image noise. With this figure, the PWLS $+S_{2+1}$ offers performance similar to conventional PWLS. The proposed PWLS$+S_{2+1}$ and boundary information performs better than the other methods at all variance levels.

Similarly, Fig. 12 plots the bias in the mean of each tumor volume of interest. This figure of merit provides insight into the accuracy of the activity values in the whole tumor volume (not just max value of tumor). Once again, the PWLS $+S_{2+1}$ and boundary information offers the best performance at most noise levels. When the global penalty is less (right half of plot), the boundary information method performs poorly. This can be expected because the boundary penalty varies throughout the image from 100% to 10% of the global value. At the edges of tumors, 10% of a low global penalty essentially under regularizes these regions, allowing more extreme fluctuations in these edge values that contribute erroneous values to the mean tumor value calculation (does not influence the max value calculation as heavily).

C. NEMA IEC phantom

Figure 13 contains reconstructions of the NEMA IEC phantom. The FBP reconstruction used a 10 mm Hanning filter and the PWLS methods used β values to regularize the images such that they have standard deviations in the background voxels that match the FBP reconstruction. Figure 14 plots the bias in the mean of the sphere activity concentration values versus sphere size for these reconstructions. Conventional PWLS and FBP have similar bias values considering noise regularization was matched in the background and was enforced in a uniform manner throughout the image. The use of just the new system model (PWLS$+S_{2+1}$) only slightly improves quantitation, a result in keeping with Figs. 11 and 12. The use of both improved system modeling and anatomical information reduced the bias in the mean values of each sphere by on average 12% for this measured data.

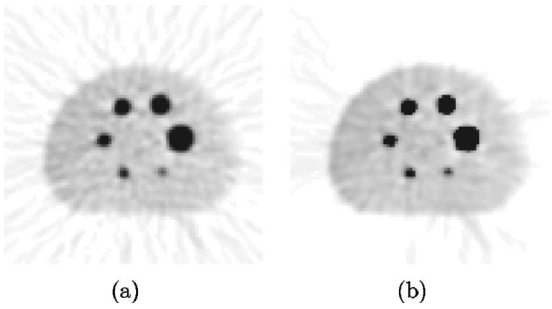

FIG. 13. Reconstructed images of measured NEMA IEC phantom using conventional FBP (a) and the proposed method with system modeling and boundary information (b).

VI. CONCLUSIONS

An improved system model and aligned anatomical information was successfully incorporated into a reconstruction algorithm and tested with simulated data. Individual reconstructions highlighted strong quantitative benefits of using the improved SRF and using known boundary information. The quantitative analysis across multiple realizations and at a variety of image smoothing levels reveals improvements with the PWLS$+S_{2+1}$ method and particularly with the PWLS$+S_{2+1}$ and boundary information method. Specifically, at one clinically relevant noise level, the PWLS$+S_{2+1}$ and boundary information method reduces the bias of maximum tumor values at the same image variance by 11% in comparison to FBP and by 5% in comparison to conventional PWLS. Likewise, this proposed method reduces the bias of mean tumor values by 8% in comparison to FBP and by 4% in comparison to conventional PWLS. Positive results from

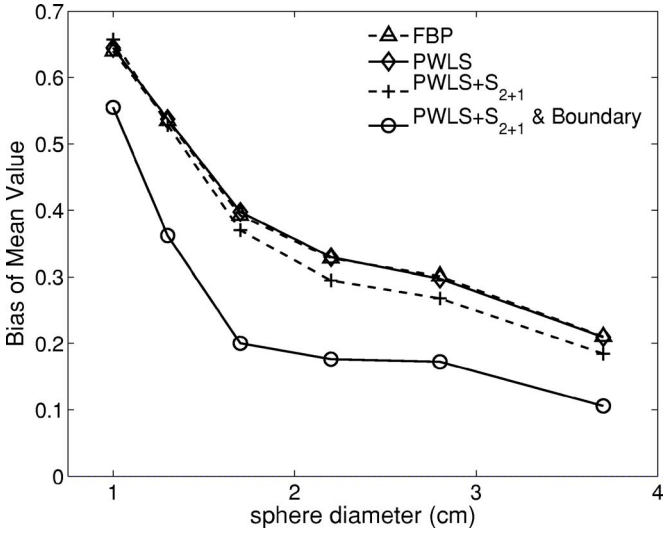

FIG. 14. Error in mean of sphere values versus sphere size for reconstructions of measured NEMA IEC phantom.

measured studies (12% reduction of mean tumor bias) confirm these simulated results and stress the improved quantitative accuracy of the proposed method.

These methods could be utilized on modern PET/CT scanners although several open problems need to be solved. Namely, the current system model is generated solely through simulations and a scheme needs to be developed for empirical modeling on actual systems. Secondly, the use of CT scans for anatomical information raises the challenge of how to accurately segment CT images into regions of emission tracer uptake. As discussed in Sec. III there are several potential segmentation approaches for this task, but further work is needed to tailor a segmentation method for CT to PET boundaries and to assess the required accuracy of the boundary locations. A further open problem is that the improved quantitation with boundary information comes at the expense of increased variance in boundary regions. New penalty terms need to be developed to reduce the variance in these regions while preserving the edge information. The positive results presented here justify our efforts to explore solutions to these challenges.

ACKNOWLEDGMENT

This work was supported by NIH grants CA74135 and CA42593.

[a]Electronic address: aalessio@u.washington.edu; URL: http://faculty.washington.edu//aalessio

[1]T. Frese, N.C. Rouze, C. A. Bouman, K. Sauer, and G. D. Hutchins, "Quantitative comparison of FBP, EM, and Bayesian reconstruction algorithms for the IndyPET scanner," IEEE Trans. Med. Imaging **22**, 258–276 (2003).

[2]V. Selivanov, Y. Picard, J. Cadorette, S. Rodrigue, and R. Lecomte, "Detector response models for statistical iterative image reconstruction in high resolution PET," IEEE Trans. Nucl. Sci. **47**, 1168–1175 (2000).

[3]E. Mumcuoglu, R. Leahy, S. Cherry, and E. Hoffman, "Accurate geometric and physical response modelling for statistical image reconstruction in high resolution PET," in Proc. of IEEE Nucl. Sci. Symp. and Med. Imaging Conf., 1996, Vol. 3, pp. 1569–1573.

[4]G. Boning, B. Pichler, M. Rafecas, E. Lorenz, M. Schwaiger, and S. Ziegler, "Implementation of Monte Carlo coincident aperture functions in image generation of a high-resolution animal positron tomograph," IEEE Trans. Nucl. Sci. **48**, 805–810 (2001).

[5]Z. Liang, "Detector response restoration in image reconstruction of high resolution positron emission tomography," IEEE Trans. Med. Imaging **13**, 314–321 (1994).

[6]D. Strul, R. B. Slates, M. Dahlbom, S. R. Cherry, and P. K. Marsden, "An improved analytical detector response function model for multilayer small-diameter PET scanners," Phys. Med. Biol. **48**, 979–994 (2003).

[7]D. Schmitt, B. Karuta, C. Carrier, and R. Lecomte, "Fast point spread function computation from aperture functions in high-resolution positron emission tomography," IEEE Trans. Med. Imaging **7**, 2–12 (1988).

[8]K. Lee, P. E. Kinahan, J. A. Fessler, R. S. Miyaoka, M. Janes, and T. K. Lewellen, "Pragmatic fully 3D image reconstruction for the MiCES mouse imaging PET scanner," Phys. Med. Biol. **49**, 4563–4578 (2004).

[9]S. Staelens, Y. D'Asseler, S. Vandenberghe, M. Koole, I. Lemahieu, and R. V. d. Walle, "A three-dimensional theoretical model incorporating spatial detection uncertainty in continuous detector PET," Phys. Med. Biol. **49**, 2337–2350 (2004).

[10]J. Qi, R. M. Leahy, S. R. Cherry, A. Chatziioannou, and T. H. Farquhar, "High-resolution 3D Bayesian image reconstruction using the microPET small-animal scanner," Phys. Med. Biol. **43**, 1001–1013 (1998).

[11]E. Veklerov, J. Llacer, and E. Hoffman, "MLE reconstruction of a brain phantom using a Monte Carlo transition matrix and a statistical stopping rule," IEEE Trans. Nucl. Sci. **35**, 603–607 (1998).

[12]A. Alessio and P. Kinahan, "PET image reconstruction," in *Nuclear Medicine*, edited by Henkin *et al.* (Elsevier, Philadelphia, 2006), Vol. 1.

[13]J. Fessler, N. Clinthorne, and W. Rogers, "Regularized emission image reconstruction using imperfect side information," IEEE Trans. Nucl. Sci. **39**, 1464–1471 (1992).

[14]G. Gindi, M. Lee, A. Rangarajan, and I. Zubal, "Bayesian reconstruction of functional images using anatomical information as priors," IEEE Trans. Med. Imaging **12**, 670–680 (1993).

[15]X. Ouyang, W. Wong, V. E. Johnson, X. Hu, and C. Chen, "Incorporation of correlated structural images in PET image reconstruction," IEEE Trans. Med. Imaging **13**, 627–640 (1994).

[16]J. Bowsher *et al.*, "Bayesian reconstruction and use of anatomical *a priori* information for emission tomography," IEEE Trans. Med. Imaging **15**, 673–686 (1996).

[17]C. Comtat *et al.*, "Clinically feasible reconstruction of 3D whole-body PET/CT data using blurred anatomical labels," Phys. Med. Biol. **47**, 1–20 (2002).

[18]A. Alessio, P. Kinahan, and T. Lewellen, "Modeling and incorporation of system response functions in 3D whole body PET," IEEE Trans. Med. Imaging **25**, 828–837 (2006).

[19]T. Lewellen, R. Harrison, and S. Vannoy, "The SimSET program in Monte Carlo calculations," in *Monte Carlo Calculations in Nuclear Medicine*, edited by M. Ljungberg, S. Strand, and M. King (IOP Publishing, Philadelphia, 1998), pp. 77–92.

[20]M. Defrise, P. Kinahan, D. Townsend, C. Michel, M. Sibomana, and D. Newport, "Exact and approximate rebinning algorithms for 3D PET data," IEEE Trans. Med. Imaging **16**, 145–158 (1997).

[21]P. M. Cheng *et al.*, "Post-reconstruction partial volume correction in PET/CT imaging using CT information," in *Radiological Society of North America*, Chicago, 2004.

[22]M. Brown, M. McNitt-Gray, J. Goldin, R. Suh, J. Sayre, and D. Aberle, "Patient-specific models for lung nodule detection and surveillance in CT images," IEEE Trans. Med. Imaging **20**, 1242–1250 (2001).

[23]W. Kostis, A. Reeves, D. Yankelevitz, and C. Henschke, "Three-dimensional segmentation and growth-rate estimation of small pulmonary nodules in helical CT images," IEEE Trans. Med. Imaging **22**, 1259–1274 (2003).

[24]V. Caselles, R. Kimmel, G. Sapiro, and C. Sbert, "Minimal surfaces: a geometric three dimensional segmentation approach," Numer. Math. **77**, 423–451 (1997).

[25]A. Tsai *et al.*, "A shape-based approach to the segmentation of medical imagery using level sets," IEEE Trans. Med. Imaging **22**, 137–154 (2003).

[26]S. Pathak, V. Chalana, D. Haynor, and Y. Kim, "Edge-guided boundary delineation in prostate ultrasound images," IEEE Trans. Med. Imaging **19**, 1211–1219 (2000).

[27]Y. E. Erdi *et al.*, "Radiotherapy treatment planning for patients with non-small cell lung cancer using positron emission tomography (PET)," Radiother. Oncol. **62**, 51–60 (2002).

[28]L. J. Vanuytsel *et al.*, "The impact of 18F-FDG positron emission tomography lymph node staging on the radiation treatment volumes in patients with non-small cell lung cancer," Radiother. Oncol. **55**, 317–324 (2000).

[29]J. Bradley *et al.*, "Impact of FDG-PET on radiation therapy volume delineation in non-small-cell lung cancer," Int. J. Radiat. Oncol., Biol., Phys. **59**, 78–86 (2004).

[30]J. Fessler, "Penalized weighted least-squares image reconstruction for positron emission tomography," IEEE Trans. Med. Imaging **13**, 290–299 (1994).

[31]C. A. Bouman and K. Sauer, "A unified approach to statistical tomography using coordinate descent optimization," IEEE Trans. Image Process. **5**, 480–492 (1996).

[32]C. Comtat, P. Kinahan, M. Defrise, C. Michel, C. Lartizien, and D. Townsend, "Simulating whole-body PET scanning with rapid analytical methods," IEEE Nuclear Science Symposium **3**, 1260–1264 (1999).

[33]T. DeGrado, T. Turkington, J. Williams, C. Stearns, J. Hoffman, and R. Coleman, "Performance characteristics of a whole-body PET scanner," J. Nucl. Med. **35**, 1398–1406 (1994).

[34]K. Zasadny and R. Wahl, "Standardized uptake values of normal tissues at pet with 2-[fluorine-18]-fluoro-2-deoxy-d-glucose: variations with body weight and a method for correction," Radiology **189**, 847–850 (1993).

[35]J.-S. Liow and S. Strother, "Practical tradeoffs between noise, quantitation, and number of iterations for maximum likelihood-based reconstructions," IEEE Trans. Med. Imaging **10**, 563–571 (1991).